From Hours to Seconds: Towards 100x Faster Quantitative Phase Imaging via Differentiable Microscopy

Udith Haputhanthri 1,2 , Kithmini Herath 2 , Ramith Hettiarachchi 2 , Hasindu Kariyawasam 2 , Azeem Ahmad 3 , Balpreet S. Ahluwalia 3 , Chamira U. S. Edussooriya 2,* , and Dushan N. Wadduwage 1,*

- ¹Center for Advanced Imaging, Faculty of Arts and Sciences, Harvard University, Cambridge, USA
- ²Department of Electronic and Telecommunication Engineering, University of Moratuwa, Sri Lanka
- ³UiT The Arctic University of Norway
- *Corresponding authors: chamira@uom.lk; wadduwage@fas.harvard.edu

ABSTRACT

With applications ranging from metabolomics to histopathology, quantitative phase microscopy (QPM) is a powerful label-free imaging modality. Despite significant advances in fast multiplexed imaging sensors and deep-learning-based inverse solvers, the throughput of QPM is currently limited by the speed of electronic hardware. Complementarily, to improve throughput further, here we propose to acquire images in a compressed form such that more information can be transferred beyond the existing electronic hardware bottleneck. To this end, we present a learnable optical compression-decompression framework that learns content-specific features. The proposed differentiable optical-electronic quantitative phase microscopy ($\partial \mu$) first uses learnable optical feature extractors as image compressors. The intensity representation produced by these networks is then captured by the imaging sensor. Finally, a reconstruction network running on electronic hardware decompresses the QPM images. The proposed system achieves compression of \times 64 while maintaining the SSIM of \sim 0.90 and PSNR of \sim 30 dB. The promising results demonstrated by our experiments open up a new pathway for achieving end-to-end optimized (i.e., optics and electronic) compact QPM systems that provide unprecedented throughput improvements.

1 Introduction

Among the label-free imaging modalities, quantitative phase microscopy (QPM) is a simple but a powerful approach, providing important biophysical information by quantifying optical phase differences^{1,2}. From the phase map, one can further yield quantitative information about the morphology and dynamics of the examined specimens^{3,4}. In addition to morphology, the measured phase maps can be converted to dry mass of the cells with accuracy that is of the order of femtograms per squared microns^{5,6}. QPM has found many important applications in biomedicine⁷ including pathogen screening⁸, cancer cell classification⁹, and label-free analysis of histopathology specimens^{10,11}. Importantly, label-free histopathology based on QPM have shown to capture subtle, nanoscale morphological properties of tissues that could lead to early detection of cancer¹². This technique also preserves the tissue sample for further molecular specific pathological analysis¹³. Moreover, recently quantitative phase imaging has even been extended to image the structures of thick biological systems such as zebra fish larval¹⁴. QPM has also been demonstrated for stain-free quantification of chromosomal dry mass in living cells¹⁵, quantification of different growth phases of chondrocytes¹⁶, identification of biophysical markers of sickle cell drug responses¹⁷ and quantification of nuclear mechanical properties that may play roles in cancer metastasis¹⁸.

The first step towards quantitative phase imaging was taken by Zernike's phase contrast microscopy ¹⁹. Phase contrast microscopy converts the phase shifts induced by the refractive indices and depth differences in the specimen into detectable intensity variations. They introduced a phase filter which directly displays phase information by interfering scattered light with a reference light beam. Even though the work improved with several extensions^{20,21}, due to the non-linear dependency between phase and the intensity, direct phase contrast techniques are incapable of quantitative phase measurements. QPM techniques overcome this problem by computational inverse reconstruction⁷. A typical quantitative phase microscope consists of an optical system (forward model) and a computational phase retrieval algorithm (inverse model)²². The forward optical system converts undetectable phase information into detectable fringe patterns; from the fringe patterns, the inverse reconstruction algorithm retrieves phase and intensity maps of the specimen. Recent developments in QPM have mostly been focused on improving the inverse reconstruction using GPU acceleration^{23–25}, deep-learning-based inverse solvers^{26–31}, and illumination patterns

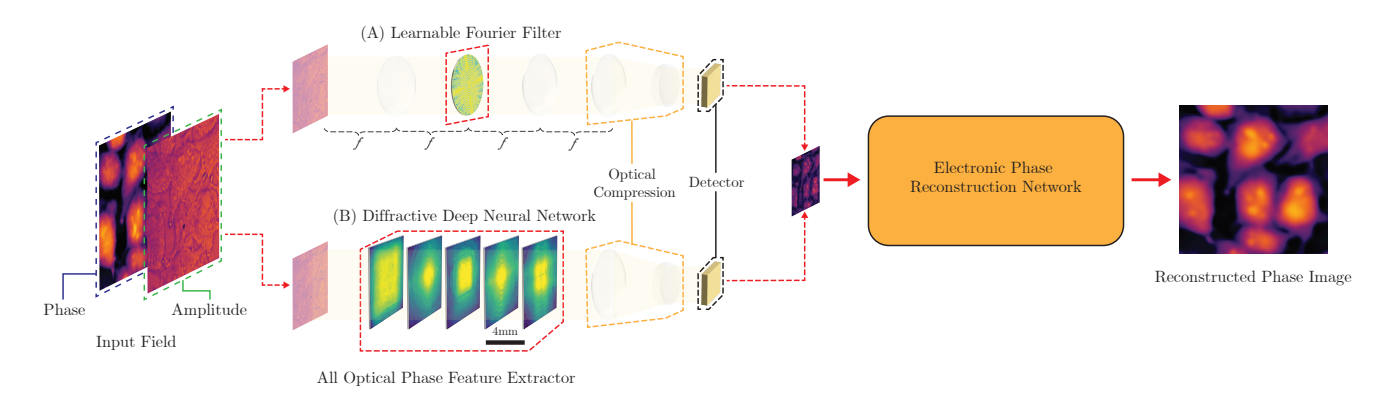


Figure 1. End-to-end pipeline: Input field with high contrast phase information is fed into the proposed optical phase feature extraction network. The resultant compressed output intensity field which contains the phase features is captured by the detector. The electronic phase reconstruction network utilizes these features to reconstruct phase information.

optimization^{32,33} (we include a comprehensive discussion on related work in the supplementary).

Orthogonal to the current developments, the main bottleneck of QPM based imaging cytometry is the image acquisition speed, which is fundamentally governed by the pixel rate of image sensors. Currently, the pixel rate of a state-of-the-art camera is around 1×10^{10} pixels/sec. However, the pixel throughput of the front-end optics is virtually unlimited. An image passes through optics at the speed of light and has been the rationale for developing optical signal processing technologies³⁴. Here we propose to exploit this property to optically compress an image in order to measure the compressed form of the image using a high-speed light detector (such as a high-speed camera). Thus the pixel throughput of the original image would be increased at a rate proportional to the degree of compression. Compressive imaging of biological specimens has been demonstrated before, using random sampling of the linearly projected image space³⁵. Better compression, however, may be achieved through learning dataset specific features of images. To this end, here we propose differentiable microscopy (∂u) to identify important image features for compression, learned through machine learning approaches³⁶. First, we modeled the compression and de-compression as a single auto-encoder neural network. Afterwards, with a large set of target images, we trained the neural network to find a low dimensional compressed representation of the images. Once trained, the decoder part of the network acts as a decompression algorithm. We then translate the encoder part of the network to optics to be used as an optical phase feature extractor. More specifically, the optical phase feature extractor encodes phase information at the compressed latent intensity field. The intensity field is then acquired by a photo detector array. The detected intensity feature map is decoded as the phase image by an electronic phase reconstruction network.

Our optical phase feature extractor is motivated by the previous work on retrieving the phase information through learnable optics (i.e. all-optical)³⁷. This work modeled phase retrieval as an optimization problem where optical network's physical parameters are optimized by minimizing the pixel-distance between input phase and the output intensity. There, the authors concluded that *A linear all-optical network is not sufficient for phase to intensity conversion for QPI datasets with higher phase values and high frequency content*. We believe that the major limitation of this previous work is the lack of *non-linearity* of the all-optical method. In contrast, here we treat the all-optical linear network as *a feature extractor* which can extract features from both phase and amplitude of the input field. The optical model only has to learn a faithful representation that contains sufficient information to reconstruct the original phase. Combining this all-optical phase feature extractor with the non-linear phase reconstruction network, we realize an *end-to-end-learnable non-linear function* for the phase retrieval task. In the following sections, first, we formulate this proposed $\partial \mu$: differentiable optical-electronic QPM as a learning problem (section 2.1). Second, we assess the feasibility of phase retrieval using linear compression and non-linear decompression functions (section 2.2). Third, we demonstrate *Compressed QPM* using an optical encoder and an electronic decoder. We use learnable Fourier filters (LFFs)³⁷ or PhaseD2NNs³⁷ as the optical feature extractors. We use SwinIR³⁸, a state-of-the-art super-resolution pipeline, as the electronic reconstruction network. Our extensive experiments with experimental datasets suggest that the proposed method can perform orders of magnitude faster QPM than the current state of the art through $\times 64 - \times 256$ compression.

2 Results

2.1 End-to-End Differentiable Microscopy for Quantitative Phase Imaging

We model the QPM system as a combination of an optical and electronic network that learns the task of reconstructing phase information of the input light field at the output of the electronic network. The optical network converts useful morphological features to an intensity field which is then captured by the detector array placed at the output plane of this network. Then, the electronic network constructs the phase map of the input light field from the captured features. This task is embedded in a loss function, and the entire network is parameterized in a differentiable manner. The parameters of the network are optimized to reduce the loss for a particular dataset. We follow a 3-stage optimization criteria for the improved stability for the end-to-end optimization; 1) optimize the all-optical phase extraction network; 2) optimize the electronic phase reconstruction network; 3) end-to-end fine-tuning.

Optimize the all-optical phase extraction network. Here the optical network is optimized to reconstruct phase at its intensity. For an input optical field $x_{in} = A_{in}e^{j\phi_{in}}$ we train an optical model H_O through which the input field is propagated to produce the output field $x_{out} = A_{out}e^{j\phi_{out}} = H_O(x_{in})$. The **phase reconstruction loss**, \mathcal{L}_{ϕ} introduced in previous work³⁷ is utilized here as,

$$\mathcal{L}_{\phi} = \mathbb{E}_{x_{in} \sim P_Y} \left[L1(|A_{out}|^2, \phi_{in}/(2\pi)) \right], \tag{1}$$

where, P_X , and L1(.) respectively represent the probability distribution of phase objects and the L1 loss.

Optimize the electronic phase reconstruction network. At this stage, we consider the end-to-end network, however, only the weights of the electronic network are optimized. The pretrained optical network discussed earlier is utilized as a feature extractor to encode input phase. We demagnify the output field of the optical network to compress the intensity representation. The electronic super-resolution network reconstructs the input phase from the compressed intensity representation. The reconstructed phase information is given by $\hat{\phi} = H_E(D(|A_{out}|^2))$. Here $H_E(.)$ and D(.) represent the electronic phase reconstruction network and the optical demagnification layer, respectively. D(.), the optical demagnification layer is implemented through a stack of 2×2 average pooling operations³⁹. Similar to previous work³⁸, we consider \mathcal{L}_{swin} , a combination of loss functions for this optimization,

$$\mathcal{L}_{swin} = \mathbb{E}_{x_{in} \sim P_X} \left[L1(\hat{\phi}, \phi_{in}/(2\pi)) + \mathcal{L}_{perceptual}(\hat{\phi}, \phi_{in}/(2\pi)) + \mathcal{L}_{adversarial}(\hat{\phi}, \phi_{in}/(2\pi)) \right], \tag{2}$$

where, $\mathcal{L}_{perceptual}$ and $\mathcal{L}_{adversarial}$ represents the perceptual loss³⁸ and adversarial loss³⁸, respectively.

End-to-end fine-tuning. As the final stage, we finetune the entire optical-electronic network to reconstruct the phase at the output of the network. With the goal of improving the reconstruction in terms of capturing fine cell structures, we incorporate the negative structural similarity index measure (SSIM)⁴⁰ as the loss function as follows,

$$\mathscr{L}_{SSIM} = \mathbb{E}_{x_{in} \sim P_X} - \frac{1}{M} \sum_{j=1}^{M} \frac{(2\mu_{X_j}\mu_{Y_j} + C_1)(2\sigma_{X_j}Y_j + C_2)}{\left(\mu_{X_j}^2 + \mu_{Y_j}^2 + C_1\right)\left(\sigma_{X_j}^2 + \sigma_{Y_j}^2 + C_2\right)},\tag{3}$$

where, X_j and Y_j represent equal-sized windows from a normalized input phase image $(\phi_{in}/2\pi)$ and the corresponding reconstructed phase output $(\hat{\phi})$, respectively, for M number of windows for an image. P_X represents the probability distribution of input phase objects. $\mu_{X_j}, \mu_{Y_j}, \sigma_{X_j}, \sigma_{Y_j}, \sigma_{X_j}, \sigma_{X_j}, \sigma_{X_j}$ are the means, variances and the covariance of the X_j and Y_j windows, respectively. $C_1 = (k_1 \times L)^2$ and $C_2 = (k_2 \times L)^2$ are regularization parameters with L = 1.0, $k_1 = 0.01$ and $k_2 = 0.03$.

In our formulation, since the input to the model is a complex-valued optical field, we only require input optical fields as training data. For the experiments, we utilized optical fields that are experimentally measured from phase objects. We considered a HeLa Cell dataset. The optical fields in this dataset (i.e. full fields of view (full FoVs)) were $250\mu m \times 250\mu m$. We considered each full FoV as 789×789 pixel grid where each pixel is 316.4 nm $\times 316.4$ nm. The dataset with full FoVs was divided into train, validation, and test sets. We cropped full FoVs into 256×256 sized patches (i.e. patch FoVs) for the end-to-end training of the proposed methods. Further details of the dataset are presented in the materials and methods (section 5). Using the above loss functions and training data, we trained optical-electronic networks that consisted of either an LFF or a PhaseD2NN as the optical network in the pipeline. To further improve the realisticity of the proposed method, we also experimented in the presence of detector noise. In the next sections we discuss these models and their results.

2.2 Linear Encoding Does not Degrade Compressibility

The optical feature extractor is a linear system. We therefore, first established the feasibility of linear compression in comparison to nonlinear compressor models.

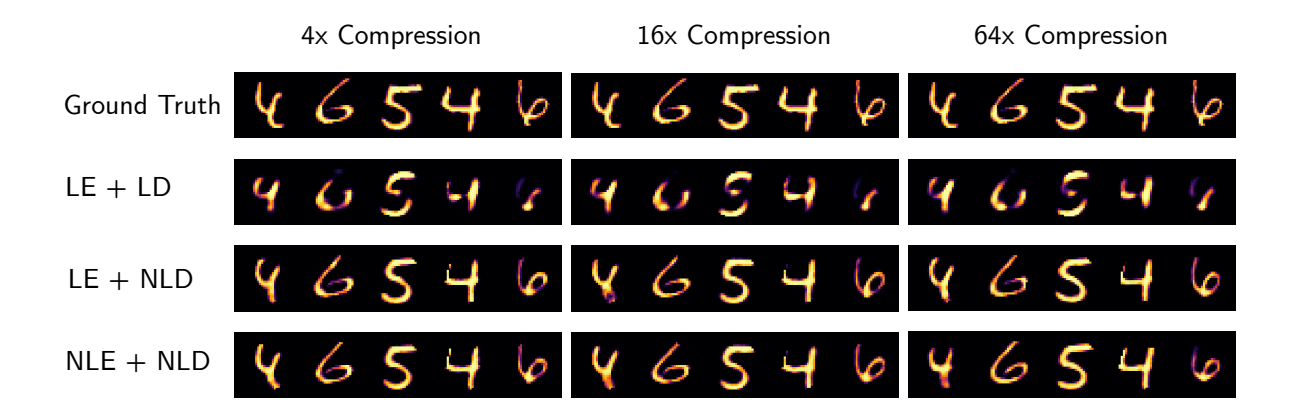


Figure 2. Compressibility of MNIST images using autoencoders (AE) with linear (L) and nonlinear (NL) encoder (E)/ decoder (D). LE, LD, NLE, and NLD represent linear encoder, linear decoder, non-linear encoder, and non-linear decoder respectively.

Linear Encoding and Non-linear Decoding Allow Compression. Prior to experimentation with an optical-electronic neural network, we first mimic the computational capabilities of the optics-based encoder and electronics-based decoder. Due to the linear nature of the optical encoder, we experimented on an autoencoder (AE) network⁴¹ consisting of a *linear encoder* followed by a *non-linear decoder*. The reconstruction results obtained from this network were compared with a fully linear autoencoder, and a fully nonlinear autoencoder. The qualitative results in Fig. 2 show that the autoencoder network comprised of a *linear encoder* and *non-linear decoder* performs on par with the fully nonlinear autoencoder.

Complex-valued Linear Encoding and Non-linear Decoding Allow Compression of Phase Information. While we have assessed the computational feasibility of a linear encoder followed by a non-linear decoder to perform reconstruction, in QPM, another main hurdle is that information of interest is in the phase of the light field. Therefore, we further assessed the ability of an autoencoder network (complex-valued linear encoder + non-linear decoder) to extract, compress and reconstruct *information encoded in the phase*. Similar to previous results, Fig. 3 shows that a complex-valued linear encoder with a nonlinear decoder has achieved similar qualitative performance as the complex-valued nonlinear encoder and nonlinear decoder.

These results suggest the computational feasibility for a linear optical network (encoder) followed by a nonlinear electronic network (decoder) to reconstruct information in the phase of the light field.

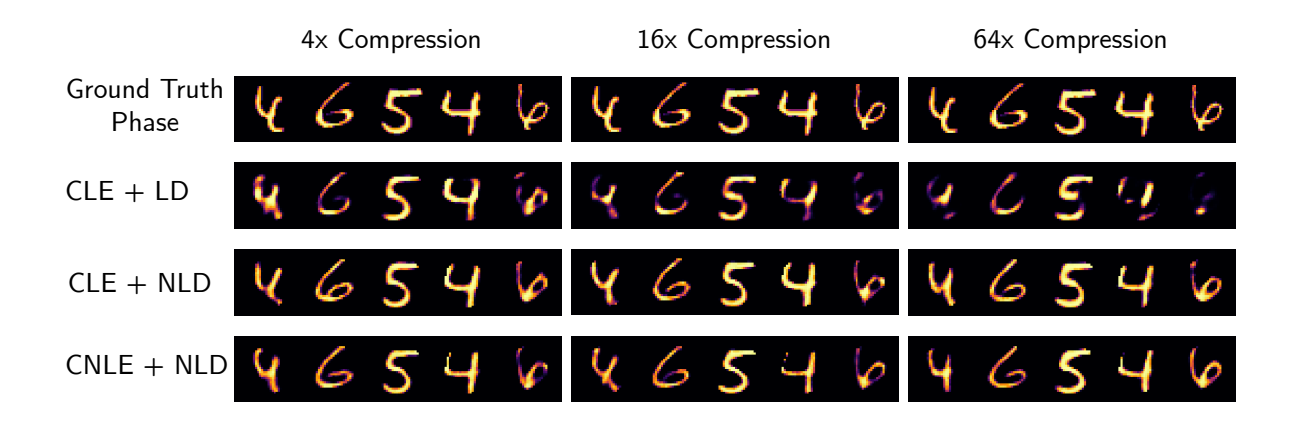


Figure 3. Phase to intensity conversion and compressibility of MNIST images using linear (L) and nonlinear (NL) encoder (E)/ decoder (D). Note that both the encoders are complex-valued hence denoted as CLE and CNLE.

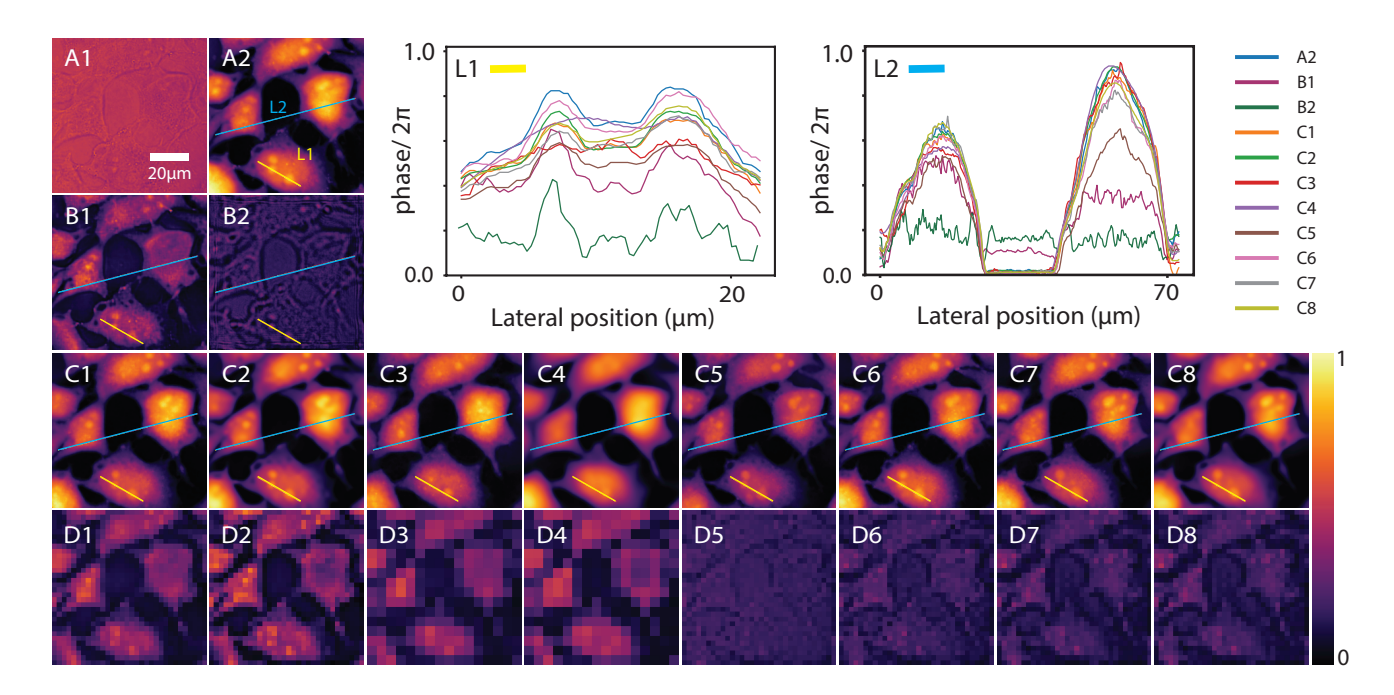


Figure 4. Qualitative performance comparison: Amplitude of input field (A1), phase of the input field (A2) (i.e. patch FoV) from the test set, all-optical phase to intensity conversion results³⁷ (i.e. baselines) using LFF (B1), PhaseD2NN (B2), Phase reconstructions from our approach 1: LFF + SwinIR with ×64 compression without fine-tuning (C1), with fine-tuning (C2), LFF with ×256 compression without fine-tuning (C3), with fine-tuning (C4), Phase reconstructions from our approach 2: PhaseD2NN + SwinIR with ×64 compression without fine-tuning + 1 optical layer (C5), without fine-tuning + 3 optical layers (C6), without fine-tuning + 5 optical layers (C7), with fine-tuning + 5 optical layers (C8), Corresponding compressed output intensity fields of optical feature extractor (D1-8). Phase values along the L1, L2 lines showing the local and global resolving power of the proposed methods.

2.3 Optical Encoding and Electronic Decoding Enable Compressed QPM

Our results in section 2.2 show that an autoencoder with a linear encoder and a non-linear decoder (*AE:LE+NLD*) can reconstruct images as good as a fully nonlinear model. In this section, we propose our model with an all-optical feature extractor (linear encoder) and an electronic super-resolution network (non-linear decoder) for QPM.

Learnable Fourier Filter (LFF) + SwinIR. Based on previous work³⁷, we first used an LFF as the optical feature extraction network. This contained an optical 4-f system with a learnable circular Fourier filter. Similar to previous work³⁷, the transmission coefficients of the circular Fourier filter were treated to be learnable. The input and output fields were 256×256 squared aperture grids. The circular Fourier filter had a radius of 128 grid points. The coefficients of the filter were randomly initialized. We used SwinIR³⁸, a state-of-the-art super-resolution network, as the electronic reconstruction network. We observed that directly training the end-to-end model (optical and electronic) was not ideal as the gradient flow between the optical and electronic networks was weak. Therefore, we employed the 3-stage criteria for the optimization of the end-to-end model as explained in section 2.1. We considered compression levels $\times 64$ and $\times 256$ for the compressed optical output intensity field in our experiments.

Table 1 shows the performances at \times 64, \times 256 compression levels. For each compression level, performances are reported with and without the fine-tuning step. The corresponding qualitative results are shown in Figs. 4 and 5. All proposed methods outperformed all-optical baselines (B1, B2) with a significant margin in terms of SSIM (structural similarity index) and PSNR (peak signal-to-noise ratio)⁴². End-to-end fine-tuning showed a considerable improvement in the performance for all the cases. Our best method achieved PSNR= 29.76 dB, SSIM= 0.90 performance at \times 64 compression, indicating that the proposed method is suitable for high-throughput QPM. Even at \times 256 compression, the proposed method still outperformed the baselines by a considerable margin with PSNR= 27.62 dB and SSIM= 0.83. To improve the realisticity of the proposed method, we further included a noise model consisting of Poisson noise and read noise³⁶. Specifically, we further fine-tuned the best model (C2) with the noise injection. A read noise with standard deviation of 6.0, and a detector maximum photon count of 10000 were used as the detector noise specifications. The proposed method with detector noise (E1) performed on par with the best

Experiment	Detector Noise	Optical Net	Compression	Finetune	# layers	full FoV/ patch FoV Metrics PSNR SSIM	
	All optical LFF				16.1565/	0.5880/	
B1					16.9761	0.6008	
D2	All optical PhaseD2NN					12.3730/	0.3163/
B2						12.6631	0.3320
C1		LFF	64	X	-	23.8267/	0.8225/
CI						25.7840	0.8278
C2				✓	-	27.2579/	0.8967/
C2						29.7608	0.9031
C3	X		256	X	-	22.5457/	0.7470/
CJ						23.9536	0.7548
C4				✓	-	26.0003/	0.8223/
CŦ						27.6129	0.8302
C5			64	X	1	22.6495/	0.7808/
CS		Phase-				23.8566	0.7889
C6		D2NN			3	24.7560/	0.8224/
00		D21111				26.0716	0.8313
C7					5	24.8015/	0.8107/
Ο,						26.0551	0.8185
C8				1	5	25.8617/	0.8519/
						27.2449	0.8602
E1	✓	LFF	64	✓	-	27.3794/	0.8935/
						29.8110	0.8998
E2		Phase- D2NN	64	✓	5	25.7665/	0.8477/
						27.0651	0.8558

Table 1. Performance comparison: Best results for optical feature extraction networks **LFF**, **PhaseD2NN** are highlighted. These best models were further fine-tuned end-to-end with the detector noise simulation (noise specifications of the detector: read noise standard deviation= 6.0, maximum photon count= 10000) to improve realisticity. We calculated the patch and full FoV metrics on the test patch FoVs and full FoVs respectively. We reconstruct the full FoVs by tiling the reconstructed patch FoVs.

model indicating that our LFF + SwinIR QPM is robust to real-world noise conditions. We further discuss the effect of the detector noise in section 3.

PhaseD2NN + SwinIR. Second, we used a PhaseD2NN³⁷ as the optical network in the proposed end-to-end framework. Similar to the previous section, SwinIR super-resolution network was used as the electronic reconstruction network. We selected the operating range of the PhaseD2NN as the visible wavelength ($\lambda = 632.8$ nm). The optical network consisted of 5 optical layers each having 256×256 optical neural grid. The size of each neuron was $\frac{\lambda}{2} \times \frac{\lambda}{2}$ (316.4 nm \times 316.4 nm). Therefore, the size of the optical layer was 80.9984μ m $\times 80.9984\mu$ m. Optical layers were separated with 3.373μ m distance between each other. The distance between the input plane and the first optical layer was 3.373μ m while the distance between the last optical layer and the detector plane was 5.904μ m. Since the pixel size matches the PhaseD2NN neuron size, we can train the end-to-end network directly on the patch FoVs from the dataset. We followed the optimization criteria presented in section 2.1 for the end-to-end training. Notably, we observed that the step-1 PhaseD2NN training in the optimization criteria was not stable due to the large number of physical parameters with a larger grid size (e.g., 256×256). To increase the stability and gradient flow of this optimization step, we considered a sub-optimization-schedule in algorithm 1. We compressed the output intensity from the optical model $\times 64$ to obtain a higher throughput.

Table 1 shows the performances for ×64 compression level. We report the performances while selecting different desired

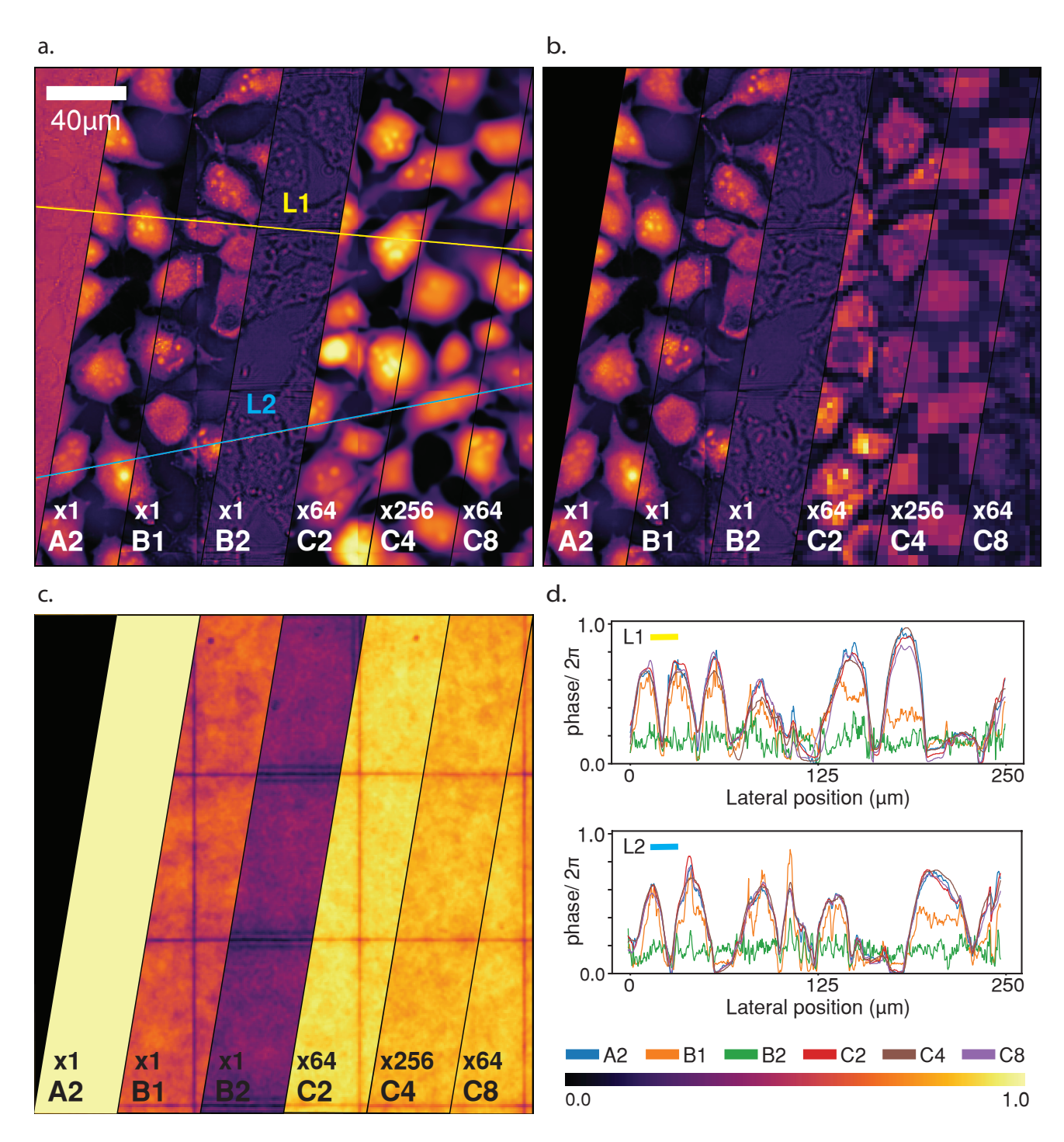


Figure 5. Performance comparison of best methods: The phase reconstructions (a), compressed intensity fields at the detector (b), SSIM maps of reconstructions (c), the resolving power of the phase reconstructions (d) are shown. Phase of the input field (A2) of a full FoV from the test set, all-optical phase to intensity conversion results³⁷ (i.e. baselines) using LFF (B1), PhaseD2NN (B2), Phase reconstructions from our approach 1: LFF + SwinIR with \times 64 compression, with fine-tuning (C2), LFF with \times 256 compression with fine-tuning (C4), phase reconstructions from our approach 2: PhaseD2NN + SwinIR with \times 64 compression, with fine-tuning + 5 optical layers (C8).

layers of the PhaseD2NN as the output layer. The corresponding learned power value is given by the algorithm 1 (more details are in the section 3). The final model with 5 layers was fine-tuned according to the proposed optimization steps.

Algorithm 1 Sub-optimization-schedule for stable all-optical PhaseD2NN training

```
Data: P_X
Result: H_O^*(.);
                                                                                    /* Optimal PhaseD2NN all-optical model */
H_O(.) \leftarrow (f_n \circ f_{n-1} \circ ... \circ f_1)(.);
                                                                                   /* Define PhaseD2NN. f_n is the n^{th} layer */
                                                                   /* Define learnable power values for each layer */
P_1, P_2, .., P_n \leftarrow 1.0;
for i \in [1, n] do
     Initializing optimizers, schedulers
      for each epoch do
          for each data batch x_{in} \sim P_X do
               A_{out} = ||P_i \times (f_i \circ f_{i-1} \circ \dots \circ f_1)(x_{in})||
               \mathcal{L}_{\phi} calculated according to section 2.1
               f_i^*, P_i^* = \operatorname{argmin}(\mathcal{L}_{\phi})
          end
     end
     if i \neq 1 then
          Initializing optimizers, schedulers
           for each epoch do
               for each data batch x_{in} \sim P_X do
                    A_{out} = ||P_i \times (f_i \circ f_{i-1} \circ \dots \circ f_1)(x_{in})||
                    \mathscr{L}_{\phi} calculated according to section 2.1
                   f_i^*, f_{i-1}^*, ..., f_1^*, P_i^* = \underset{f_i, f_{i-1}, ..., f_1, P_i}{\operatorname{argmin}} (\mathcal{L}_{\phi})
               end
          end
     end
end
```

Similar to section 2.3, fine-tuning improved the performance. We explored different number of diffractive layers for the PhaseD2NN without the fine-tuning step and the results are presented in Table 1. We performed further experiments with a 5 layer PhaseD2NN (C8 and E2). Our method achieved the best performance of PSNR= 27.24 dB, SSIM= 0.86 with $\times 64$ compression which is considerably higher than the baselines. Similar to the previous section, we injected detector noise with similar specifications of a maximum photon count of 10000 and detector read noise standard deviation of 6.0. The resultant performance with the detector noise (E2) was on par with the best model without the noise (C8). This indicates that our PhaseD2NN + SwinIR QPM is robust to real-world noise conditions. Further experiments with detector noise are presented in section 3.

3 Discussion

Overall Comparison. Fig. 5 represents the qualitative results for best performing models. Fig. 5(d) shows that the proposed differentiable optical-electronic QPM systems have higher resolving capability compared to all-optical baselines. Fig. 5(c) SSIM maps show how our methods perform for different regions of full FoV. Low SSIM in edges indicate that there is room to improve the proposed QPM just by refining the edges of generated patches. We observe that, even though both proposed methods: 1) LFF + SwinIR; 2) PhaseD2NN + SwinIR outperform the all-optical baselines with a considerable margin, the LFF based method performs better than the PhaseD2NN + SwinIR in terms of SSIM and PSNR. Even though this is the case with the performance, one can note that PhaseD2NN based method has the more compact footprint compared to the LFF-based method.

Stability of PhaseD2NN Training. We observed that the optimization step 1, i.e., all-optical reconstruction (see section 2.1), was not stable for the PhaseD2NN. We further observed that the reason for this instability was the larger patch FoV (e.g. 256×256) and the large number of learnable parameters. To overcome this, we used a sub-optimization-schedule for the PhaseD2NN training motivated by progressive growing learning principles⁴³. The proposed schedule is presented in algorithm 1. Instead of training the PhaseD2NN in an end-to-end fashion for all optical phase reconstruction, here we optimize the PhaseD2NN layer by layer progressively with the phase reconstruction loss. With this schedule, we were able to create a path to flow gradients through the optical network. Even though it can be argued that the proposed schedule leads to a

	Noise		full FoV/ patch FoV		
Optical Net	Specific	ations	metrics		
	max.				
	photon	σ_{read}	PSNR	SSIM	
	count				
	100	4	23.4928/	0.777/	
	100		25.0266	0.7834	
LFF		6	22.5004/	0.7606/	
			24.1487	0.7663	
	10000	4	27.4122/	0.8935/	
	10000		29.8110	0.8997	
		6	27.3794/	0.8935/	
			29.8110	0.8998	
	100	4	17.8942/	0.6441/	
Phase-	100		18.7526	0.6502	
D2NN		6	16.8953/	0.6094/	
DZININ			17.7111	0.6158	
	10000	4	25.7193/	0.8478/	
	10000		27.0456	0.8559	
	6		25.7665/	0.8477/	
			27.0651	0.8558	

Table 2. Performance of our method for different detector noise conditions: Our best models (C2, C8 in table 1) are further fine-tuned with the corresponding noise specifications.

sub-optimal solution, we achieved quantitatively sufficient performance for QPM³¹. After training the all-optical PhaseD2NN, we considered outputs from the layers 1, 3 and 5 for the experiments discussed in section 2.3.

Resolving Power of Differentiable Optical-Electronic QPM. We analyze the resolving power of the proposed differentiable optical-electronic QPM in Fig. 4(d). The plots demonstrate the phase value variations along lines L1 and L2 on the patch FoV. Phase variations along L1 and L2 further shows the superior resolving ability of the proposed methods for local and global features respectively. Furthermore, fine-tuning improves the resolving capability for most of the models.

Effect of Photodetector Noise. To further evaluate the behaviour of the proposed method with detector noise, we evaluated the method with maximum photon counts of 100 and 10000, and read noise standard deviations of 4.0 and 6.0. Table 2 shows that differentiable optical-electronic QPM is robust to noise when the maximum photon count is 10000. We note that for most QPM applications high light conditions can be used. Even though the proposed method performed worse for lower photon counts (e.g., 100), it still performed far better than all-optical baselines. We further noticed that the performance degradation due to higher read noise is insignificant for larger photon counts (e.g., 10000).

4 Conclusion

QPM is an emerging label-free imaging modality with a wide range of biological and clinical applications. Recent advances in QPM are focused on developing fast instruments through better detectors and fast deep-learning-based inverse solvers. However, currently, the QPM throughput is fundamentally limited by the pixel throughput of the imaging detectors. Orthogonal to current advances, to improve QPM throughput beyond the hardware bottleneck, here we propose to use content-aware compressive data acquisition. Specifically, we utilize an LFF or a PhaseD2NN to extract compressed phase features. A state-of-the-art super-resolution deep network then decodes the captured information to quantitatively reconstruct the phase image. Therefore, the proposed pipeline inherently improves the imaging speed while achieving high quality reconstructions ($SSIM \sim 0.90, PSNR \sim 30 \text{ dB}$) even at a ×64 compression level. Additionally, considering compact PhaseD2NNs, our QPM technique can potentially lead to front end QPI systems that can be deployed in smaller form factors at micrometer to millimeter scale. We believe such systems with compact front end optical compressors may find vital applications in label-free in-vivo cancer diagnostics and in-vivo brain imaging of small animal models. Moreover, the advances presented in this work may lead to similar developments in a wide-range of label-free coherent imaging modalities such as photothermal, coherent anti-stokes Raman scattering (CARS), and stimulated Raman scattering (SRS).

5 Methods

5.1 Datasets

We acquired and used a HeLa dataset³⁷ for our experiments. We followed the sample preparation procedure explained in previous work³⁷. The initial dataset contained 501 complex-valued images (i.e. detected FoVs). Each detected FoV was obtained by a camera with a 2304 \times 2304 pixel grid where the pixel size is 6.5 μ m \times 6.5 μ m. The light field that comes from the specimen was magnified \times 60 before projecting it onto the detector.

To obtain the dataset, we first calculated the side length of the light fields before the magnification (= $\frac{2304pixels \times 6.5 \ \mu m/pixel}{60}$ = 249.6 μ m). Second, we calculated the number of 316.4 nm ×316.4 nm sized pixels in these light fields (= round($\frac{249.6 \ \mu m}{316.4 \ nm/pixel}$ = 789pixels)). Finally we resized the detected FoVs (i.e. 2304 × 2304 pixel grids) into 789 × 789 pixel grids. This results in the light field before the magnification with a pixel size of 316.4 nm ×316.4 nm. We call these FoVs full FoVs. We obtained train, validation, and test sets by dividing the full FoV dataset into 401, 50, and 50 sets. For the training of the proposed networks, we considered 256 × 256 cropped patches (i.e. patch FoVs) from the full FoVs.

5.2 Implementation Details

We implemented the proposed optical-electronic networks with Python version 3.6.13. We considered auto differentiation in PyTorch⁴⁴ framework version 1.8.0 for the joint optimization/ training of the proposed optical-electronic networks. We conducted all experiments on a server with 12 Intel(R) Xeon(R) Platinum 8358 (2.60 GHz) CPU Cores, an NVIDIA A100 Graphical Processing Unit with 40 GB memory running on the centos operating system.

We considered batch size 32, learning rates of 0.1, 0.001 for LFF and PhaseD2NN all-optical feature extractor optimization (i.e., optimization stage 1) respectively. LFF was trained for 1500 epochs with multi-step learning rate scheduler⁴⁴ (milestones : [50, 400, 650, 1000, 1400], $\gamma = 0.1$). PhaseD2NN was trained for 1500 epochs after each optimizer initialization step in algorithm 1. For joint multi-layer optimizations in algorithm 1, learning rate 0.00005 was used for better stability. For the optimization stage 2, we followed similar training configurations used in SwinIR³⁸. Lastly, for the final optimization stage (i.e. end-to-end fine-tuning), we fine-tuned the LFF + SwinIR and PhaseD2NN + SwinIR for 24000 and 3000 epochs with learning rate of 5×10^{-6} , respectively. We used Adam⁴⁵ as the optimizer for all optimizations.

References

- **1.** Popescu, G., Ikeda, T., Dasari, R. R. & Feld, M. S. Diffraction phase microscopy for quantifying cell structure and dynamics. *Opt. Lett.* **31**, 775–777, DOI: 10.1364/OL.31.000775 (2006).
- **2.** Park, Y., Popescu, G., Badizadegan, K., Dasari, R. R. & Feld, M. S. Diffraction phase and fluorescence microscopy. *Opt. Express* **14**, 8263–8268, DOI: 10.1364/OE.14.008263 (2006).
- **3.** Fang-Yen, C. *et al.* Imaging voltage-dependent cell motions with heterodyne mach-zehnder phase microscopy. *Opt. Lett.* **32**, 1572–1574, DOI: 10.1364/OL.32.001572 (2007).
- **4.** Amin, M. S. *et al.* Microrheology of red blood cell membranes using dynamic scattering microscopy. *Opt. Express* **15**, 17001–17009, DOI: 10.1364/OE.15.017001 (2007).
- **5.** Sung, Y. *et al.* Three-dimensional holographic refractive-index measurement of continuously flowing cells in a microfluidic channel. *Phys. Rev. Appl.* **1**, 014002, DOI: 10.1103/PhysRevApplied.1.014002 (2014).
- **6.** Choi, W. et al. Tomographic phase microscopy. Nat Methods **4**, 717–719 (2007).
- **7.** Park, Y. K., Depeursinge, C. & Popescu, G. Quantitative phase imaging in biomedicine. *Nat. Photonics* **12**, 578–589, DOI: 10.1038/s41566-018-0253-x (2018).
- 8. Jo, Y. et al. Holographic deep learning for rapid optical screening of anthrax spores. Sci Adv 3, e1700606 (2017).
- **9.** Roitshtain, D. *et al.* Quantitative phase microscopy spatial signatures of cancer cells. *Cytom. Part A* **91**, 482–493, DOI: 10.1002/cyto.a.23100 (2017).
- **10.** Majeed, H. *et al.* Quantitative histopathology of stained tissues using color spatial light interference microscopy (cslim). *Sci. Reports* **9**, DOI: 10.1038/s41598-019-50143-x (2019).
- **11.** Rivenson, Y. *et al.* PhaseStain: The digital staining of label-free quantitative phase microscopy images using deep learning. *Light. Sci. Appl.* **8**, DOI: 10.1038/s41377-019-0129-y (2019).
- **12.** Wang, Z., Tangella, K., Balla, A. & Popescu, G. Tissue refractive index as marker of disease. *J Biomed Opt* **16**, 116017 (2011).

- **13.** Cree, I. A. *et al.* Guidance for laboratories performing molecular pathology for cancer patients. *J Clin Pathol* **67**, 923–931 (2014).
- **14.** Kandel, M. *et al.* Epi-illumination gradient light interference microscopy for imaging opaque structures. *Nat. Commun.* **10**, DOI: 10.1038/s41467-019-12634-3 (2019).
- **15.** Sung, Y., Choi, W., Lue, N., Dasari, R. R. & Yaqoob, Z. Stain-free quantification of chromosomes in live cells using regularized tomographic phase microscopy. *PLoS One* **7**, e49502 (2012).
- **16.** Sung, Y. *et al.* Size homeostasis in adherent cells studied by synthetic phase microscopy. *Proc. Natl. Acad. Sci. United States Am.* **110**, DOI: 10.1073/pnas.1315290110 (2013).
- **17.** Hosseini, P. *et al.* Cellular normoxic biophysical markers of hydroxyurea treatment in sickle cell disease. *Proc Natl Acad Sci U S A* **113**, 9527–9532 (2016).
- **18.** Singh, V. *et al.* Studying nucleic envelope and plasma membrane mechanics of eukaryotic cells using confocal reflectance interferometric microscopy. *Nat. Commun.* **10**, DOI: 10.1038/s41467-019-11645-4 (2019).
- 19. Zernike, F. Observation of transparent objects. *Physica* 974–986 (1942).
- 20. Glückstad, J. Phase contrast image synthesis. Opt. Commun. 130, 225–230, DOI: 10.1016/0030-4018(96)00339-2 (1996).
- **21.** Shibata, N. *et al.* Differential phase-contrast microscopy at atomic resolution. *Nat. Phys.* **8**, 611–615, DOI: 10.1038/nphys2337 (2012).
- **22.** Jo, Y. J. *et al.* Quantitative phase imaging and artificial intelligence: A review. *IEEE J. Sel. Top. Quantum Electron.* **25**, DOI: 10.1109/JSTQE.2018.2859234 (2018).
- 23. Kim, K., Kim, K. S., Park, H., Ye, J. C. & Park, Y. Real-time visualization of 3-d dynamic microscopic objects using optical diffraction tomography. *Opt. Express* 21, 32269–32278, DOI: 10.1364/OE.21.032269 (2013).
- **24.** Lim, J. *et al.* Comparative study of iterative reconstruction algorithms for missing cone problems in optical diffraction tomography. *Opt. Express* **23**, 16933–16948, DOI: 10.1364/OE.23.016933 (2015).
- **25.** Sung, Y. *et al.* Optical diffraction tomography for high resolution live cell imaging. *Opt. InfoBase Conf. Pap.* **17**, 1977–1979, DOI: 10.1364/ntm.2009.ntua2 (2009).
- **26.** Nguyen, T., Bui, V. & Nehmetallah, G. Computational optical tomography using 3d deep convolutional neural networks (3d-dcnns). *Opt. Eng.* **57**, DOI: 10.1117/1.OE.57.4.043111 (2018).
- **27.** Di, J., Wang, K., Li, Y. & Zhao, J. Deep learning-based holographic reconstruction in digital holography. In *Imaging and Applied Optics Congress*, HTu4B.2, DOI: 10.1364/DH.2020.HTu4B.2 (Optica Publishing Group, 2020).
- **28.** Zhu, Y., Yeung, C. H. & Lam, E. Y. Digital holographic imaging and classification of microplastics using deep transfer learning. *Appl. Opt.* **60**, A38–A47, DOI: 10.1364/AO.403366 (2021).
- **29.** Wang, K., Kemao, Q., Di, J. & Zhao, J. Y4-net: A deep learning solution to one-shot dual-wavelength digital holographic reconstruction. *Opt. Lett.* **45**, 4220–4223, DOI: 10.1364/OL.395445 (2020).
- **30.** Wang, H., Lyu, M. & Situ, G. eholonet: A learning-based end-to-end approach for in-line digital holographic reconstruction. *Opt. Express* **26**, 22603–22614, DOI: 10.1364/OE.26.022603 (2018).
- **31.** Wang, K., Dou, J., Kemao, Q., Di, J. & Zhao, J. Y-net: A one-to-two deep learning framework for digital holographic reconstruction. *Opt. Lett.* **44**, 4765–4768, DOI: 10.1364/OL.44.004765 (2019).
- **32.** Kellman, M. R., Bostan, E., Repina, N. A. & Waller, L. Physics-based learned design: Optimized coded-illumination for quantitative phase imaging. *IEEE Transactions on Comput. Imaging* **5**, DOI: 10.1109/tci.2019.2905434 (2019).
- **33.** Matlock, A. & Tian, L. High-throughput, volumetric quantitative phase imaging with multiplexed intensity diffraction tomography. *Biomed. Opt. Express* **10**, 6432–6448, DOI: 10.1364/BOE.10.006432 (2019).
- **34.** Yeh, P. & Gu, C. *Landmark Papers on Photorefractive Nonlinear Optics* (World Scientific, 1995). https://www.worldscientific.com/doi/pdf/10.1142/2067.
- **35.** Studer, V. *et al.* Compressive fluorescence microscopy for biological and hyperspectral imaging. *Proc. Natl. Acad. Sci.* **109**, E1679–E1687, DOI: 10.1073/pnas.1119511109 (2012). https://www.pnas.org/doi/pdf/10.1073/pnas.1119511109.
- **36.** Haputhanthri, U., Seeber, A. & Wadduwage, D. Differentiable microscopy for content and task aware compressive fluorescence imaging, DOI: 10.48550/ARXIV.2203.14945 (2022).
- **37.** Herath, K. *et al.* Differentiable microscopy designs an all optical quantitative phase microscope, DOI: 10.48550/ARXIV. 2203.14944 (2022).

- **38.** Liang, J. *et al.* Swinir: Image restoration using swin transformer. 2021 IEEE/CVF Int. Conf. on Comput. Vis. Work. (ICCVW) 1833–1844 (2021).
- 39. Gholamalinezhad, H. & Khosravi, H. Pooling methods in deep neural networks, a review. ArXiv abs/2009.07485 (2020).
- **40.** Wang, Z., Bovik, A., Sheikh, H. & Simoncelli, E. Image quality assessment: From error visibility to structural similarity. *IEEE Transactions on Image Process.* **13**, 600–612, DOI: 10.1109/TIP.2003.819861 (2004).
- **41.** Wang, Y., Yao, H. & Zhao, S. Auto-encoder based dimensionality reduction. *Neurocomputing* **184**, 232–242, DOI: https://doi.org/10.1016/j.neucom.2015.08.104 (2016). RoLoD: Robust Local Descriptors for Computer Vision 2014.
- **42.** Horé, A. & Ziou, D. Image quality metrics: PSNR vs. SSIM. In 2010 20th International Conference on Pattern Recognition, 2366–2369, DOI: 10.1109/ICPR.2010.579 (2010).
- **43.** Karras, T., Aila, T., Laine, S. & Lehtinen, J. Progressive growing of gans for improved quality, stability, and variation. *ArXiv* **abs/1710.10196** (2018).
- **44.** Paszke, A. *et al.* Pytorch: An imperative style, high-performance deep learning library. In Wallach, H. *et al.* (eds.) *Advances in Neural Information Processing Systems 32*, 8024–8035 (Curran Associates, Inc., 2019).
- 45. Kingma, D. & Ba, J. Adam: A method for stochastic optimization. Int. Conf. on Learn. Represent. (2014).